2016

A Tomographic-PIV Investigation of Vapor-Induced Flow Structures in Confined Jet Impingement Boiling

M. J. Rau

P. P. Vlachos

S V. Garimella

A Tomographic-PIV Investigation of Vapor-Induced Flow Structures in Confined Jet Impingement Boiling[1]

Matthew J. Rau, Pavlos P. Vlachos, Suresh V. Garimella[2]

School of Mechanical Engineering, Purdue University, 585 Purdue Mall, West Lafayette, IN 47907 USA

Abstract

Tomographic particle image velocimetry (PIV) is used to study the effect of confinement gap height on the liquid flow characteristics in jet impingement boiling. This first application of tomographic PIV to flow boiling is significant given the complexity of confined two-phase jet impingement. A jet of subcooled water at a Reynolds number of 5,000 impinges onto a circular heat source undergoing boiling heat transfer at a constant heat input. Confinement gap heights of 8, 4, and 2 jet diameters are investigated. A visual hull method is used to reconstruct the time-varying regions of the vapor in the flow. The vapor motion is found to govern the liquid flow pattern and turbulence generation in the confinement gap. Time-averaged velocities and regions of turbulent kinetic energy in the liquid are highest for a confinement gap height of 8 jet diameters, with lower velocity magnitude and turbulence being observed for the smaller spacings. Coherent vortical structures identified with the λ_2-criterion are found to occur most frequently near the moving vapor interface. The most intense regions of turbulent kinetic energy do not coincide with the location of coherent structures within the flow. Irrotational velocity fluctuations in the liquid phase caused by vapor bubble pinch-off are the primary cause of the high turbulent kinetic energy measured in these regions. At a gap height of $H/d = 2$ the vapor plume is constrained as it grows from the heat source, causing bulk flow oscillations in the downstream region of the confinement gap.

[1] Submitted for consideration in *International Journal of Multiphase Flow*, February 2016
[2] Corresponding author, Tel: +1 765 494 5621. E-mail address: sureshg@purdue.edu

Keywords

two-phase jet impingement, boiling, turbulence, tomographic PIV, visual hull reconstruction, void fraction, fluorescence imaging

1. Introduction

Flow boiling heat transfer yields the high heat removal rates necessary to cool modern high-power electronics devices. Recent advances in two-phase jet impingement have demonstrated that high heat transfer coefficients can be achieved while maintaining low pressure drops that are generally insensitive to vapor quality in this flow boiling configuration (Rau and Garimella, 2014; Rau *et al.*, 2015). These characteristics make two-phase jet impingement attractive as a potential drop-in replacement for single-phase power electronics cooling arrangements.

The occurrence of phase change can complicate the design of liquid-cooled electronics packages. Vapor bubbles can modify liquid flow paths and act as a source of turbulence (Roy *et al*., 1993; Roy *et al*., 1997). One obstacle to implementation of confined two-phase jet impingement is a lack of understanding of the liquid-vapor interactions, particularly as the confinement height is reduced to the small dimensions encountered in compact electronics packaging. Understanding these liquid-vapor dynamics will aid in the avoidance of flow instabilities common to many two-phase flow systems (Boure *et al.*, 1973) and guide the design of high-performance flow boiling cooling systems.

Current understanding of the interactions between vapor bubbles and the liquid in flow boiling is primarily derived from single-point measurements, such as those obtained with laser Doppler velocimetry or hot-wire anemometry. Single-point velocity statistics are useful for determining average properties; however, linking these results to dynamic phase interactions, such as vapor-induced coherent structures, is difficult. Increases in turbulent kinetic energy observed in such two-phase flow studies have been attributed to many different factors including: liquid displacement caused by vapor bubble motion (Lance and Bataille, 1991; Roy *et al*., 1993), and increased shear stresses caused by the bubble velocity

(Theofanous and Sullivan, 1982; Serizawa and Kataoka, 1990). The dominant mechanism for turbulence enhancement due to boiling is not yet clear.

Whole-field visualization-based flow measurement methods such as particle image velocimetry (PIV) can provide the vapor bubble size, shape, and position in the flow with simultaneous liquid-phase velocimetry measurements. This allows researchers to probe the spatial flow structure. Lindken and Merzkirch (2002) used PIV to study bubbles rising in stagnant water. They detected regions of high vorticity and shear in the wake of rising bubbles. The flow structure behind bubbles oscillating laterally in an upward flow arrangement has also been captured with PIV (Brücker, 1999; Tokuhiro *et al*., 1998; 1999); the oscillations were shown to create additional vorticity in the bubble wake and a more uniform distribution of turbulent kinetic energy. Hassan *et al*. (2001) studied the three-dimensional motion of a single rising air bubble in a narrow pipe with stereo particle tracking velocimetry. The vortex structures in the wakes of the bubbles showed a lack of symmetry that resulted from the three-dimensional spiraling and rocking motion of the bubble as it rose in the liquid.

Tomographic PIV (tomo-PIV) is a technique that extends the measurement capabilities of PIV to three dimensions. These capabilities, which allow resolution of the full three-dimensionality of the flow including coherent turbulence structures, have seen much recent progress (Scarano, 2013). Time-resolved tomo-PIV, where the measurements are acquired at a high repetition rate, has been used to study the vortex dynamics of free jets (Violato and Scarano, 2011) and impinging jets (Violato *et al*., 2012), where vortical structures were shown to enhance convective heat transfer from an impinging jet formed with a chevron nozzle.

When applied to two-phase flow, time-resolved tomo-PIV allows simultaneous vapor-phase visualization with time- and space-resolved liquid velocity measurements; these high-fidelity measurement capabilities can provide fundamental insights into two-phase flow behavior that were previously not possible. Tomo-PIV has seen limited application to multiphase flows, having been primarily used to study the flow around solid objects such as fish and zooplankton (Adhikari and

Longmire, 2013, Gemmell *et al*., 2014, Adhikari *et al*., 2015, Murphy *et al*., 2012). Flow boiling has not yet been studied with tomo-PIV.

In a recent study, Rau *et al*. (2016) used time-resolved stereo-PIV to study the two-phase flow field during confined jet impingement boiling. The results showed that vapor production due to boiling modified the liquid flow at a confinement gap height of 4 jet diameters. The purpose of the current investigation is to study the effects of different confinement gap heights on the flow characteristics of two-phase jet impingement and to test the applicability of tomo-PIV to study flow boiling. A single, circular 3.75 mm-diameter (d) jet of water is studied with jet-to-target spacings (H) of 8, 4, and 2 jet diameters. The liquid flow field in the confinement gap is measured using tomo-PIV at a jet Reynolds number of 5,000 during boiling. A vapor volume reconstruction technique is presented and used to explain the relationship between vapor bubble dynamics and liquid motion in the gap. The influence of confinement gap height on coherent structures in the flow, and their relation to turbulence, is also presented.

2. Experimental Facility

The experiments are performed in a custom-developed two-phase jet impingement facility described in Rau *et al.* (2016). Key details are provided here for completeness. Water is circulated through the flow loop using a magnetically-coupled gear pump and the mass flow rate is measured by a Coriolis flow meter (CMFS015M, Emerson) with an uncertainty of ± 0.1%. The flow loop is operated in an open-loop configuration, where deionized water is boiled continuously in the reservoir while venting to the atmosphere through reflux condensers to maintain degassed conditions.

The test section remains unchanged from the previous study of Rau *et al*. (2016), and is made from polyether ether ketone (PEEK) with front and back polycarbonate walls for optical access. The jet of water is formed by a 3.75 mm diameter, 7.5 mm long sharp-edged orifice located in the center of a circular confining orifice plate mounted at the end of a plenum. Three different confinement gap heights (H), defined as the spacing between the jet orifice and impingement surface as shown in Figure 1b, are

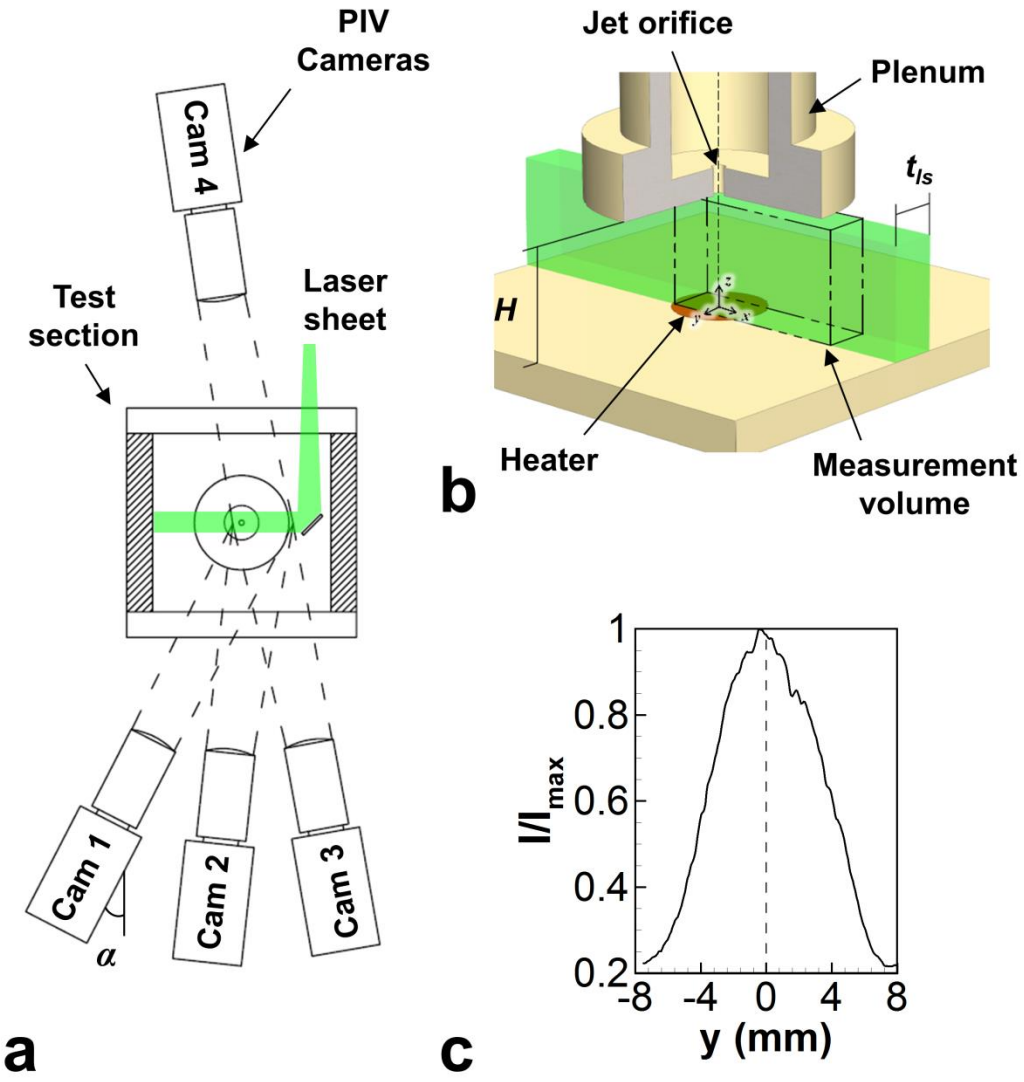

Figure 1. (a) A top-view schematic drawing of the tomo-PIV measurement system oriented around the jet impingement test section, (b) a three-dimensional cartoon of the laser illumination and measurement volume, and (c) the normalized average illumination intensity profile.

investigated: 8, 4, and 2 jet diameters. The jet impinges onto the center of a 25.4 mm-diameter gold-plated copper heat source that is mounted flush with the bottom of the test section. The confinement gap extends 9.3 jet diameters radially (r) downstream from the jet axis. Spent fluid from the impinging jet and any vapor generated from boiling exit through a return port at the top of the test section.

The jet inlet temperature is measured by a T-type thermocouple positioned just upstream of the jet orifice plate. The uncertainty in the calibrated thermocouple measurements is estimated to be ±0.3 °C. The heat source is powered by embedded cartridge heaters. The heat flux into the fluid is calculated from the electrical heat input after subtracting heat losses, which are estimated based on a numerical heat loss model (Rau and Garimella, 2014). The water saturation temperature is determined based on the pressure inside the test section chamber, maintained at 103 kPa absolute, as measured by a transducer with a 0 to 206 kPa absolute pressure range and a measurement uncertainty of ±0.3 kPa.

3. Experimental Methods

3.1. Time-resolved tomographic particle image velocimetry

Multi-camera visualization is used to provide time-resolved tomographic PIV measurements with simultaneous visualization of the vapor plume created during boiling. The PIV particles and vapor bubbles are illuminated with a high-speed Nd:YLF laser (Terra PIV, Continuum), which delivers a pulse of 527 nm light at 750 Hz. The laser beam is expanded using a beam collimator and two cylindrical lenses to form an illumination volume approximately 16 mm thick (t_{ls}). A mirror (83-536, Edmund Optics) is mounted on the bottom wall of the test section to reflect the laser light across the confinement gap, as shown in Figure 1a. The illumination volume is positioned parallel to the front and rear walls of the test section, with the jet orifice centered within the illumination thickness, as shown in Figure 1b.

PIV images are acquired with four high-speed cameras (Phantom Miro M340, Vision Research) arranged around the test section as shown in Figure 1a. The cameras are positioned on a common plane parallel to the bottom of the test section. This horizontal mounting configuration is required to image within the narrow confinement gap without obstruction. The cameras view the experiment through 105 mm lenses (Micro-Nikkor, Nikon) with apertures of *f*/11. A Scheimpflug lens-tilt adapter is used on Camera 1 (α = 30°) to align the focal plane of the camera with the illumination volume (Prasad and Jensen, 1995). A lens tilt adapter is not needed on Cameras 2, 3 and 4 due to their smaller viewing angles (α = 18, -7, and 11°, respectively) relative to the light-sheet-normal direction. The overlapping camera

views and illuminated region result in the measurement volume shown in Figure 1b. Images are acquired with a resolution of 1304 × 1600 pixels.

3.2. PIV particles for boiling water

Fluorescence illumination with long-pass optical filters is necessary to image particles in close proximity to vapor bubbles (Hassan *et al*., 1992). Fluorescent red (peak emission wavelength λ = 584 nm) polystyrene particles, 10 μm in diameter (PSF-010UM, Magsphere), are used in the current experiments. Long-pass optical filters with a 550 nm cut-on wavelength (FELH0550, Thor Labs) installed on the cameras eliminate high-intensity laser reflections from the images. The fluorescent particles, moderate light emission from the PEEK walls (Rau *et al*., 2016), and the optical filtering result in clean experimental images of *both* the PIV particles and vapor structures, as shown in Figure 5. The particle density (ρ = 1.05 g/cm^3) is close to that of water at 100 °C (ρ = 0.958 g/cm^3), which avoids particle settling in the measurement volume.

The melting temperature of polystyrene (exceeding 200 °C) is high enough to avoid melting during the experiment; however, the heat source surface does reach the glass transition temperature of the particles (107 °C, Rieger, 1996) during boiling. Particles were found to soften during experiments and allow the embedded fluorescent dye to leach out. Over time, the dye would contaminate the heated surface and cause the wetted area to become hydrophobic. A rigorous cleaning procedure is implemented to clean the heat source, test section, and flow loop prior to each boiling experiment. The heater surface is cleaned sequentially with toluene, acetone, and isopropanol. Post-experimentation, the flow loop is filtered using a 7 μm particulate filter to remove particles from the water. The test section and reservoir are then thoroughly cleaned with isopropanol and the entire flow loop is flushed with clean water. This cleaning procedure kept the heated surface from becoming hydrophobic. The surface wettability was tested prior to each experiment and remained consistent throughout testing.

3.3. Test procedure

The plenum height is adjusted to set the desired confinement gap height. Deionized water is degassed by circulating through the flow loop while boiling the water using both the inline heater and immersion heater in the reservoir. The reservoir is simultaneously vented to the atmosphere through Graham reflux condensers. After two hours of degassing, the water flow rate and power to the inline heater are adjusted to maintain a jet inlet subcooling of 10 °C and a jet Reynolds number of 5,000. Throughout the rest of the experiment, degassed conditions are maintained by continuously boiling the water in the reservoir with the immersion heater while venting through the Graham condensers.

Once a steady operating condition is reached, PIV images of the single-phase jet impingement flow field (prior to boiling) are acquired. The single-phase flow field is used for measurement validation and to serve as a baseline case for comparison with the two-phase flow field. The single-phase images are also used for the tomo-PIV self-calibration procedure. Fifty ml of degassed water is extracted from the reservoir and mixed with 5.0 ml of 2.5% w/v (weight per volume) PIV particles. This mixture is injected into the reservoir and PIV images are acquired. The open operation of the flow loop allows any air introduced into the reservoir through particle seeding to be continuously evacuated, ensuring that degassed conditions are maintained. This seeding procedure results in a uniform distribution of particles within the measurement domain, with an average particle image density of 0.02 particles per pixel. PIV images are acquired for 2.6 s, corresponding to a set of 1,985 time-resolved images. Following image acquisition, the water in the loop is filtered and the heater is then powered to the desired heat input. Particle seeding and image acquisition is repeated once steady state boiling is reached.

Rau *et al*. (2016) introduced a modified boiling number for heat flux non-dimensionalization as

$$Bl^* = \frac{q}{\dot{m} c_p \left(T_{sat} - T_j \right)}, \tag{1}$$

where q is the heat input to the fluid (after subtracting heat losses from the electrical power input), $\dot{m}$ is the mass flow rate, c_p is the specific heat, T_{sat} is the saturation temperature, and T_j is the jet inlet

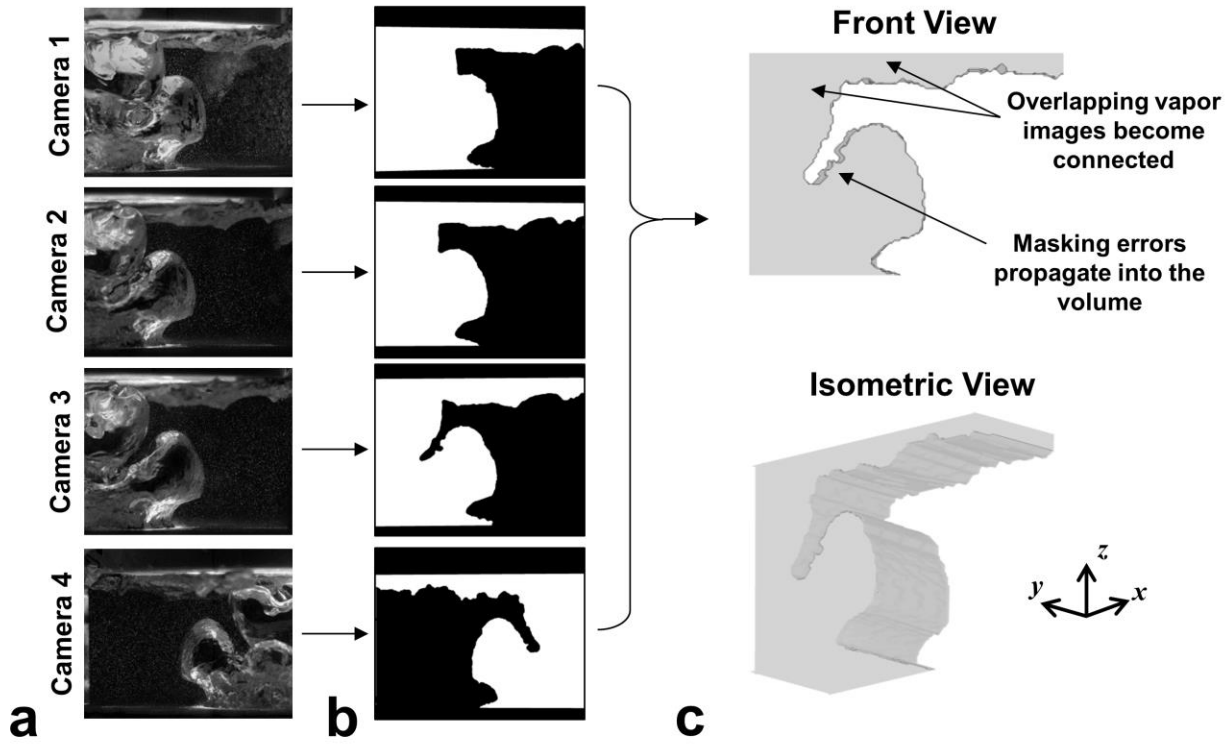

Figure 2. The visual-hull vapor reconstruction steps showing (a) the camera images, (b) mask creation, and (c) the resulting 3D vapor volume within the measurement depth.

temperature. A modified boiling number of $Bl^* = 1$ implies that saturated conditions are reached in the flow based on the heat input and sensible heat capacity of the liquid flow. The heat flux used for the current investigation represents $Bl^* = 1.5$, indicating that saturated conditions are surpassed for the boiling cases presented.

3.4. Vapor volume reconstruction

Three-dimensional bubble shapes have been reconstructed using a variety of methods in the literature. Hassan *et al*. (2001) determined the bubble centroid position and orientation from stereoscopic experimental images and fit an oblate spheroid to this position in 3D space. Fujiwara *et al*. (2004) acquired shadowgraph images of isolated bubbles from perpendicular viewing angles, allowing the

integration of the bubble shape captured in one view through the profile captured in the second view. In the current study, the vapor forms a plume-like structure above the heat source rather than a collection of discrete bubbles. A visual hull reconstruction method is chosen as it allows time-resolved vapor reconstruction directly from the tomo-PIV images.

Vapor reconstruction is performed by first masking vapor regions in each camera image, creating a binary image of each view as shown in Figure 2a and Figure 2b. The image processing steps used to create the binary masks are presented in Rau *et al*. (2016). A vapor volume is then created by projecting each camera mask using a Multiplicative Line-of-Sight (MLOS) algorithm and the camera calibration mapping functions. The resulting volume contains the intersecting regions from each camera projection. An example set of vapor image masks and the resulting visual hull-reconstructed volume is shown in Figure 2b and Figure 2c.

The visual hull reconstruction technique has been applied to the flow around falling solid objects (Adhikari and Longmire 2012) and to the study of fish and zooplankton using tomo-PIV (Adhikari and Longmire 2013; Gemmell *et al*. 2014; Adhikari *et al*. 2015; Murphy *et al*. 2012). Adhikari and Longmire (2012) described the strengths and limitations of the visual hull method when applied to tomo-PIV images. Reconstruction accuracy is limited by the number of camera views available. Fewer cameras and shallow viewing angles result in reconstructions that can be incorrectly elongated through the depth of the viewing system. The limited optical access offered by the present confined boiling geometry necessitates the use of shallow camera viewing angles. Because the vapor plume structures are wider than the illumination volume, any resulting elongation in the vapor reconstruction would cause only a reduction in curvature of the plume interface. The corresponding error in the volume due to this reduction in curvature is likely small. In contrast, this visual hull method would not be appropriate for the reconstruction of small discrete bubbles in the flow as the resulting error would be much more significant. Thus, the two-phase flow conditions in the current study are an appropriate first application for tomo-PIV using a visual hull method for vapor reconstruction.

3.5. Tomographic PIV processing

The cameras are calibrated prior to the experiments using a single-level dot-matrix target as described in Rau *et al*. (2016). The target is traversed from -10 mm to +10 mm in 1 mm increments (21 calibration planes total) through the depth of the measurement volume. Mapping functions relating the image pixel coordinates to the physical coordinates of the measurement volume are then fit to the calibration dots using a third-order polynomial function in DaVis 8 software (LaVision). A volumetric self-calibration using PIV images captured prior to boiling is also performed to refine the mapping functions as outlined by Wieneke (2008).

The PIV images are preprocessed using steps similar to those outlined by Violato *et al*. (2011) and Adhikari and Longmire (2012). The minimum gray-level intensity at each pixel, calculated from the entire image set, is first subtracted followed by subtraction of a sliding minimum calculated from a 3 × 3 pixel window. Intensities are then normalized across a 16 × 16 pixel window, and a 5 × 5 pixel Gaussian filter is applied. The resulting images have spatially uniform particle intensities with zero background intensity; these qualities are advantageous for the self-calibration and particle volume reconstruction (Elsinga *et al*., 2006; Wieneke, 2008).

Particle volumes are reconstructed using the SMART algorithm (Atkinson and Soria, 2009) implemented in DaVis 8 with five MART iterations. A reconstruction quality (Q) (defined as the normalized correlation coefficient of the exact and reconstructed particle intensity distributions) above the 0.75 threshold recommended by Elsinga, *et al*. (2006) is expected with this number of iterations given the particle seeding density and the use of four cameras. Figure 1c shows a representative average profile of the normalized particle volume intensity through the measurement depth. The Gaussian-shaped distribution of illumination from the laser light is evident for the region -8 mm < y < 8 mm. The low-intensity signal ($I/I_{max} \approx 0.2$) in the regions y < -8 mm and y > 8 mm is representative of the ghost particle intensity. Elsinga *et al*. (2006) recommend a signal-to noise ratio of 2 or more when comparing reconstructed vs. ghost particle intensity; the interrogation region in the present work is limited to -4 mm < y < 4 mm where the reconstruction meets this criterion.

The reconstructed particle volumes are cross-correlated using a multi-pass direct correlation scheme with the fluid trajectory correlation (Lynch and Scarano, 2013) in DaVis 8. Initial interrogation volumes of 96×96×96 voxels are reduced to 48×48×48 voxels with 75% overlap. The resulting velocity measurement resolution is 12 voxels (0.32 mm) in the *x*, *y*, and *z* directions. To restrict computation of velocity vectors to within the liquid regions of the domain, the 3D masking technique of Adhikari and Longmire (2012) is implemented. The vapor volume from the visual hull reconstruction is used as a 3D mask to remove velocity vectors computed within the vapor regions of the domain.

Vapor motion causes intermittent discontinuities in the time-resolved data sampling of liquid velocity. At a given time step, liquid velocities are undefined at locations in the measurement domain (*x*, *y*, *z*) occupied by vapor. As a result, locations in the domain frequently occupied by vapor have few measurements of liquid velocity; in contrast, locations with infrequent vapor presence have many measurements of liquid velocity (a maximum number of liquid velocity measurements of 1,984 are obtained from the set of PIV images in locations where vapor is never present). Time-averaged velocities are thus calculated considering the convergence of the velocity statistics at each location using only the local data sample length. This calculation is described in detail in Rau *et al*. (2016).

Uncertainty estimation for tomo-PIV has not yet reached the rigor of particle-image-based and correlation-based uncertainty estimates that have been developed for planar PIV (Timmins *et al*., 2012; Sciacchitano *et al*., 2013; Charonko and Vlachos, 2013; Xue *et al*., 2015). Instead, velocity uncertainty estimates have thus far been obtained by comparing a raw velocity time history (obtained from the tomo-PIV measurements) to a filtered version of the same velocity time history (Violato and Scarano, 2011; Violato *et al*., 2012). The standard deviation of the residual between these two velocity signals is taken as the measurement uncertainty.

In the present study, the velocity measurement uncertainty is estimated by comparing the mass flow rate measured using the PIV results within the confinement gap during single-phase operation to the mass flow rate injected into the domain by the impinging jet. The mass flow rate in the gap is calculated from the PIV measurements by integrating the average radial velocities through the measurement depth and

height, assuming axisymmetric flow conditions. The standard deviation of the difference in mass flow rates obtained by these two approaches, sampled at many radial locations within the confinement gap from results at all three confinement gap heights, yields a velocity measurement uncertainty estimate of 0.004 m/s assuming a 68.5% confidence interval. This uncertainty estimate is equivalent to a 0.2 voxel displacement and represents 1% of the jet velocity.

4. Results

In this section, tomo-PIV results are presented at three confinement gap heights, 8, 4, and 2 jet diameters. Results for single-phase operation ($Bl^* = 0$) and two-phase operation ($Bl^* = 1.5$) are discussed to clarify the relationship between vapor generation and the resulting liquid motion and turbulence induced in the confinement gap.

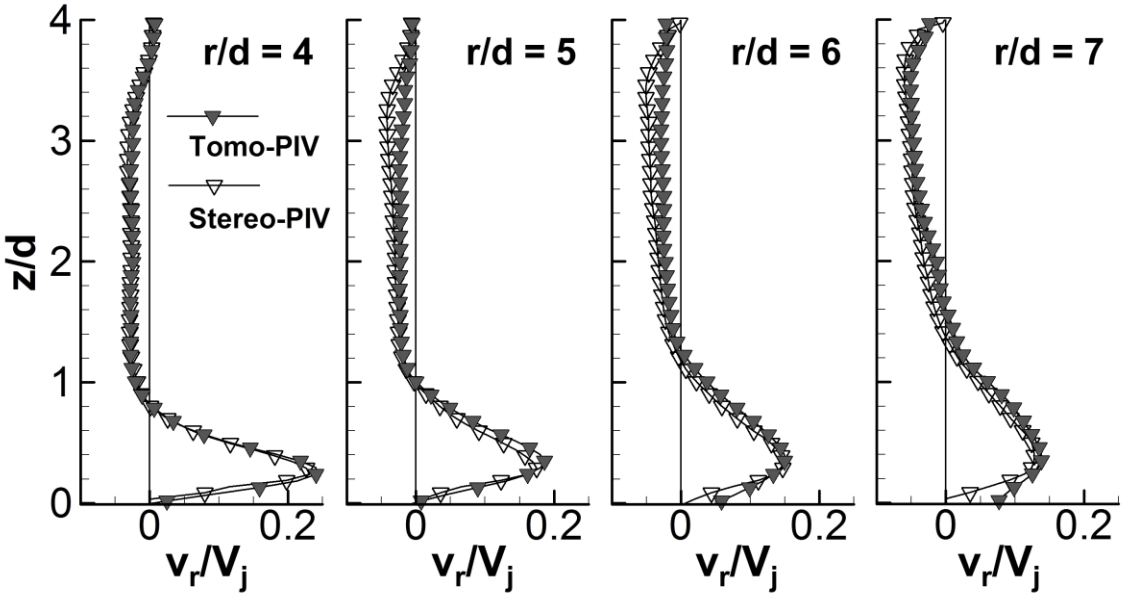

Figure 3. Average radial velocity profiles for Re = 5,000 measured with tomo-PIV compared with the stereo-PIV measurements of Rau *et al*. (2016).

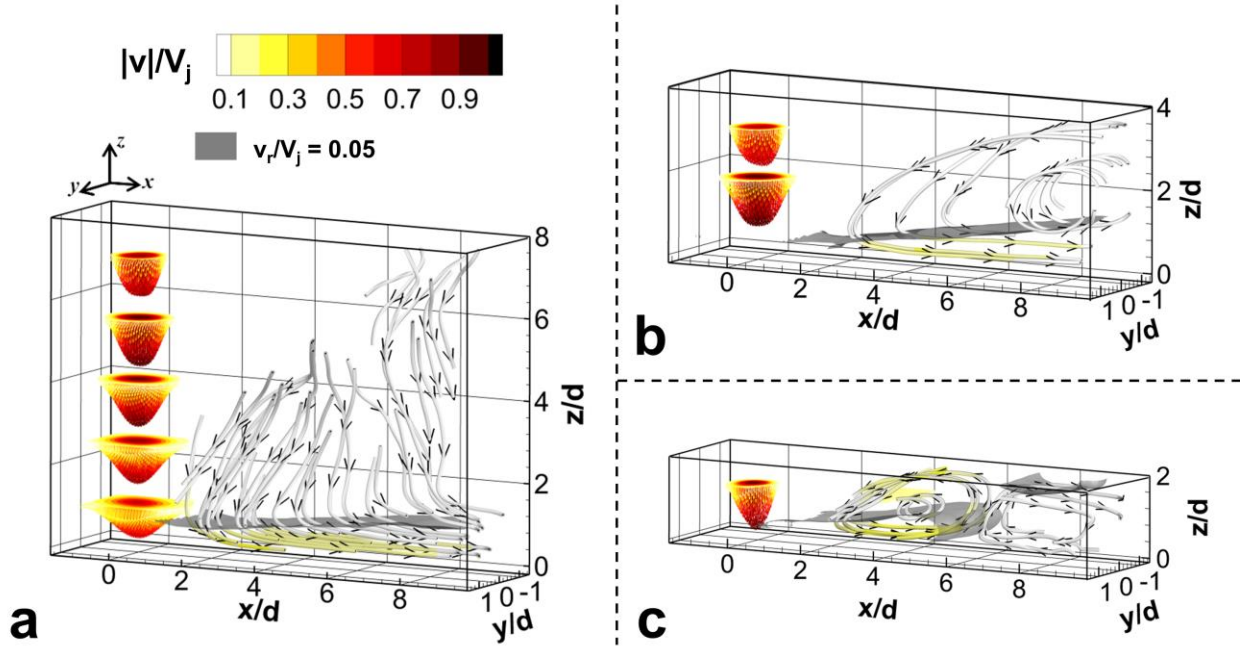

Figure 4. Time-averaged single-phase (Bl^* = 0) jet impingement flow fields for Re = 5,000 with a confinement gap height of (a) H/d = 8, (b) H/d = 4, and (c) H/d = 2. The impinging jet is shown with velocity surfaces plotted across horizontal slices, while streamtraces show the flow downstream in the confinement gap.

4.1. Single-phase impinging jet flow

Figure 3 shows time-averaged radial velocity profiles for the confinement gap height of H/d = 4 obtained from the tomo-PIV measurements of the current study in comparison to those from the stereo-PIV measurements of the same flow field reported in Rau *et al*. (2016). For the plots, the tomographic results are averaged through the measurement depth at each radial location. The profiles obtained from stereo- and tomo-PIV approaches agree very well, with the root-mean-squared difference in measured velocities falling within 2% of the jet velocity. This agreement between data from two distinct experiments, measurement systems, and data reduction algorithms lends confidence in the experimental repeatability and the validity of the tomo-PIV measurements.

Figure 4 shows the single-phase (Bl^* = 0) time-averaged flow field resulting from the single impinging jet at the three confinement gap heights studied; H/d = 8, H/d = 4, and H/d = 2. The impinging jet is shown with velocity surfaces plotted across horizontal slices where the jet velocity is greater than

5% of the jet exit velocity (V_j). Stream traces, also colored by velocity magnitude, show the flow pattern in the confinement gap. The boundary of the wall jet is indicated with the grey iso-surface plotted where $v_r/V_j = 0.05$.

At $H/d = 8$ (Figure 4a) the jet widens as it develops prior to impingement on the bottom wall. The liquid in the confinement gap is drawn towards the impinging jet and developing wall jet at a low velocity, as shown with the stream traces. A distinct counter-clockwise flow pattern is observed at $H/d = 4$ (Figure 4b). Ambient liquid enters the gap through the top half of the confinement gap and moves with a counter-clockwise motion as it is entrained into the wall jet. As the confinement gap height is reduced further to $H/d = 2$, the counter-clockwise recirculation moves inward (the core of this recirculation pattern is centered at $r/d \approx 4.8$), and a counter-recirculation zone is observed to form close to the edge of the confinement gap, centered at $r/d \approx 8$.

The confinement gap flow patterns shown in Figure 4 agree with those presented in the literature on single-phase confined impinging jets (Fitzgerald and Garimella, 1997; 1998; Rau *et al*., 2016). Fitzgerald and Garimella (1998) studied the effect of confinement on the position of the recirculation zone and showed that it moves inwards as the confinement gap height is reduced. This recirculation also causes the wall jet to separate from the bottom wall at $r/d = 4.8$ as the liquid is drawn upwards due to the recirculation at this location.

4.2. Vapor-modified flow paths

Representative experimental images of confined jet impingement boiling at $Bl^* = 1.5$ are shown for all three confinement gap heights in Figure 5. Vapor from the heat source forms a large plume-like structure over the heated surface that rises vertically before flowing outwards along the top wall of the confinement gap.

Time-averaged liquid flow paths are shown with 3D streamtraces, colored by velocity magnitude, in Figure 6. Also plotted are iso-surfaces representing the statistical location of the vapor plume. Regions occupied by vapor for 95% of the time sample or more (termed the 95% plume position) are shown in

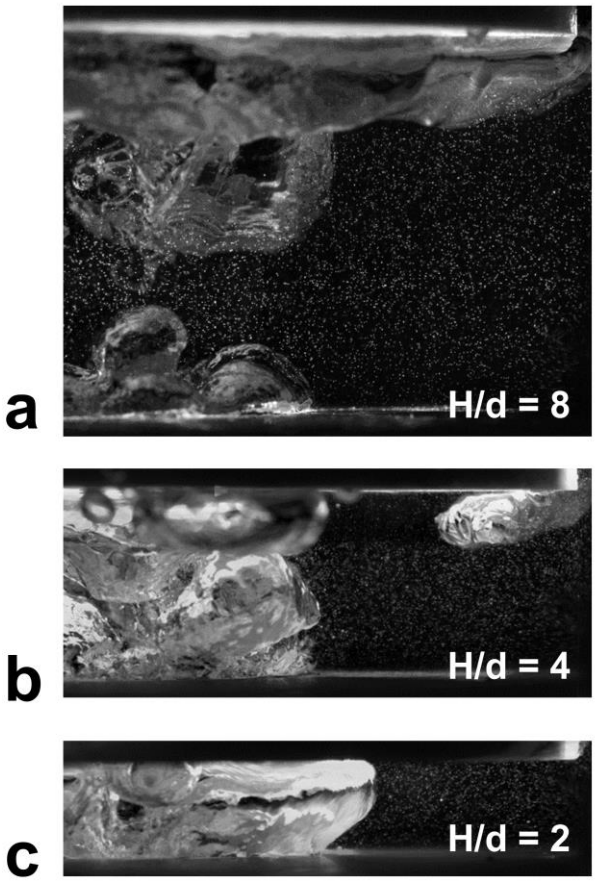

Figure 5. Representative images of boiling at Re = 5,000 and Bl^* = 1.5 for (a) H/d = 8, (b) H/d = 4, and (c) H/d = 2.

black, and regions occupied by vapor 50% of the time sample or more (termed the 50% plume position) are bounded by the grey iso-surface. This statistical mapping of the vapor phase offers a way to visualize the time-averaged plume positions extracted from the entire data sample. Similar mappings have been used in the study of gas jets submerged in water (Weiland and Vlachos, 2013).

At H/d = 8 (Figure 6a), liquid is shown to flow inward and upward towards the vapor plume. The liquid accelerates as it is drawn towards the plume with velocity magnitudes up to $|v|/V_j$ = 0.81 occurring within the 50% plume position. At the confinement gap height of H/d = 4, a similar flow pattern is observed, though ambient liquid acceleration is reduced as the maximum velocity magnitude in the gap is only $|v|/V_j$ = 0.39. The flow at H/d = 2 is predominantly outward, in contrast to the patterns observed at

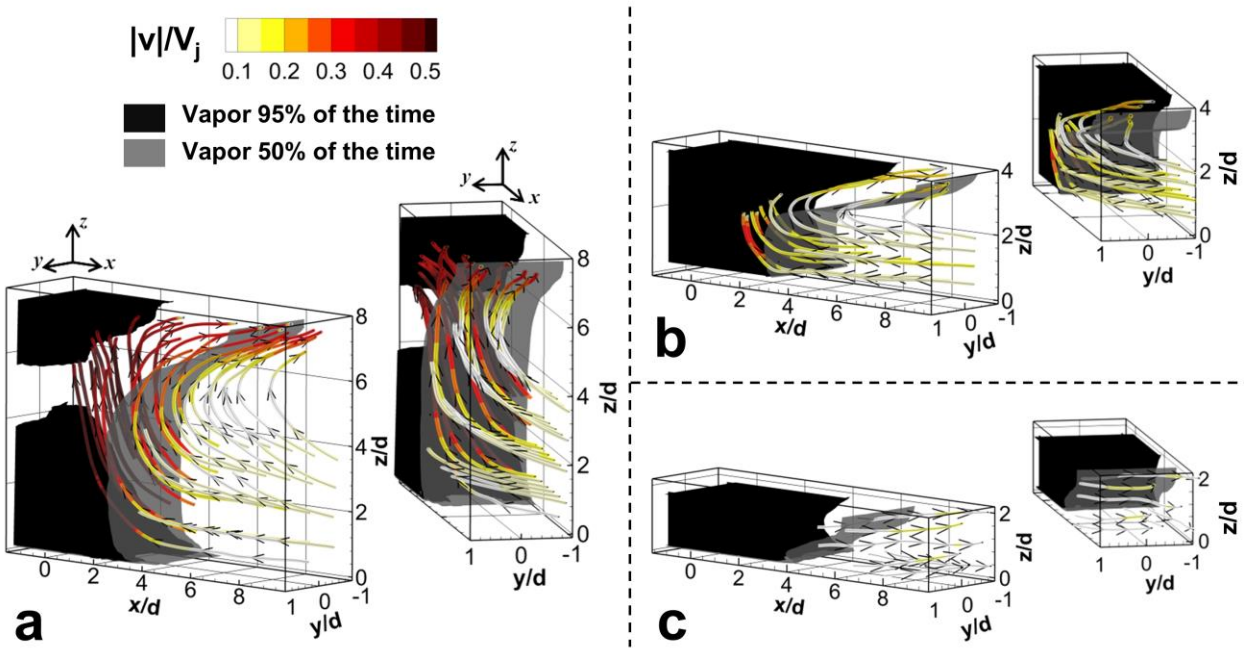

Figure 6. Time-averaged flow fields for Re = 5,000 and *Bl** = 1.5 with a confinement gap height of (a) *H*/*d* = 8, (b) *H*/*d* = 4, and (c) *H*/*d* = 2. The 50% plume position is shown with the grey iso-surfaces and the black volumes represent regions occupied by vapor 95% of the time or more. Streamtraces show the mean liquid motion.

the larger spacings. The lowest average liquid velocities occur at this spacing with a maximum velocity magnitude of $|v|/V_j = 0.20$.

The confinement gap is tall enough at *H*/*d* = 8 for the vapor plume to pinch off and separate as it rises, as shown in Figure 5a; this intermittent pinch-off results in the gap in the 95% plume position region shown in Figure 6a. In contrast, pinch-off does not occur at the smaller confinement gaps, which show a continuous 95% plume envelope. As plume pinch-off occurs, liquid fills the region previously occupied by vapor, and is then drawn upwards in the wake of the rising vapor. This motion results in the flow paths and high time-averaged velocities observed at *H*/*d* = 8 in Figure 6a.

The liquid streamtraces in Figure 6 show asymmetric liquid motion through the measurement depth. To further describe this motion, contours of circumferential velocity in the confinement gap at *H*/*d* = 8 in both single- and two-phase operation are plotted in Figure 7. Figure 7a (*Bl** = 0) shows that there is asymmetric motion in the flow even prior to boiling. Red regions in the contour indicate liquid being

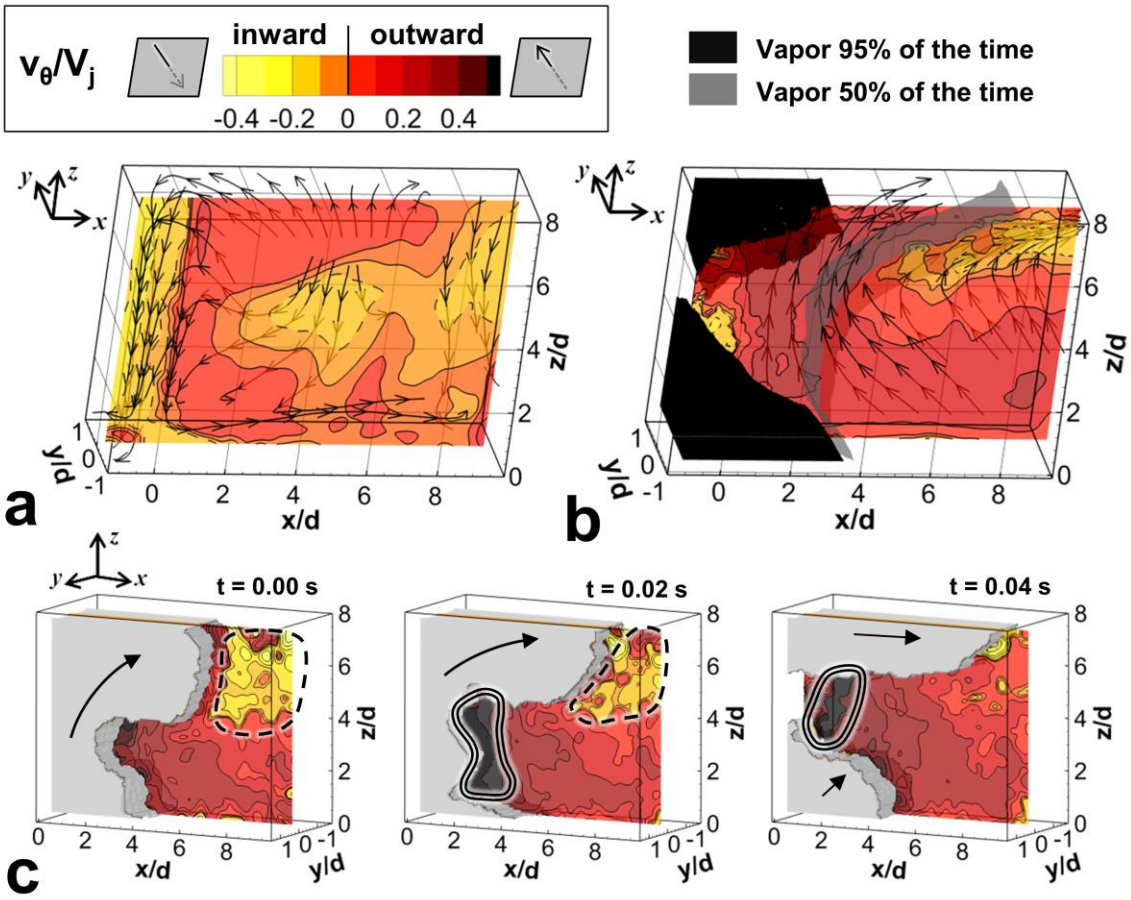

Figure 7. Circumferential velocity contours for Re = 5,000 at H/d = 8 plotted along the y/d = 0 plane showing time-averaged velocities for (a) Bl^* = 0 and (b) Bl^* = 1.5. (c) Instantaneous velocities for Bl^* = 1.5 at three time steps with vapor shown in grey and arrows indicating direction of vapor motion. Regions of high inward velocity are circled with the dashed line and regions of high outward velocity with the compound line in (c).

drawn outward (motion out of the page), while yellow and orange contours show motion inward (motion into the page). The streamtraces near the top of the confinement gap (at $z/d \approx 7.5$) display a swirling motion as liquid is entrained into the impinging jet. The swirling motion shown in Figure 7a, which is likely caused by slight asymmetries in the setup, are weak; circumferential velocities range from $-0.1 < v_\theta/V_j < 0.1$ for this single-phase flow.

Greater asymmetric liquid velocities are observed in two-phase operation. As shown in Figure 7b, outward average velocity magnitudes are greatest (reaching $v_\theta/V_j = 0.32$) inside of the 50% plume position, while a region of strong inward velocities (up to $v_\theta/V_j = -0.27$) is found near the edge of the

confinement gap at $z/d \approx 7$. The transient interaction of the vapor with the liquid is shown in the time steps presented in Figure 7c. A region of strong inward liquid velocity (indicated with the dashed line) initially occurs at the top of the confinement gap to the right of the vapor plume. Circumferential velocities of up to $v_\theta/V_j = -0.48$ occur in this region, which shrinks as the vapor moves outwards. As necking occurs in the plume prior to pinch-off, a high outward circumferential velocity develops in the necking region, shown outlined with the compound line. A maximum outward velocity of $v_\theta/V_j = 1$ is measured at $t = 0.02$ s. The dynamic evolution of the vapor plume, shown in Figure 7c, results in the higher-magnitude circumferential liquid velocities observed in two-phase operation compared to single-phase operation.

4.3. Vapor-induced turbulence

4.3.1. Turbulent kinetic energy

Contours of normalized turbulent kinetic energy (*TKE*) plotted along the $y/d = 0$ plane are shown in Figure 8, with iso-surfaces showing the most intense regions of *TKE* in the flow. Normalized *TKE* is calculated from the fluctuating radial, axial, and circumferential velocities as

$$TKE = \frac{1}{2}\left(\overline{v_r'^2} + \overline{v_z'^2} + \overline{v_\theta'^2}\right)\Big/ V_j^2 \,. \tag{2}$$

The prime denotes the fluctuating velocity component as calculated from a Reynolds decomposition, shown for the radial component as $v_r'(t) = v_r(t) - \bar{v}_r$, where $v_r(t)$ is the instantaneous radial velocity and $\bar{v}_r$ is the time-averaged radial velocity.

At the spacing of $H/d = 8$, high levels of *TKE* (reaching a maximum of 0.19) are primarily concentrated at the discontinuity in the 95% plume position, shown in Figure 8a. The intense liquid velocity fluctuations in this region are caused by the vapor plume pinch-off. *TKE* radiates outwards from this location, as indicated by the contours, and spreads along the top confinement gap wall; the liquid flow paths at this spacing (shown in Figure 4a) likely carry turbulence fluctuations in this direction. A similar *TKE* distribution is evident at $H/d = 4$ (Figure 8b), though the intense region of *TKE* coinciding

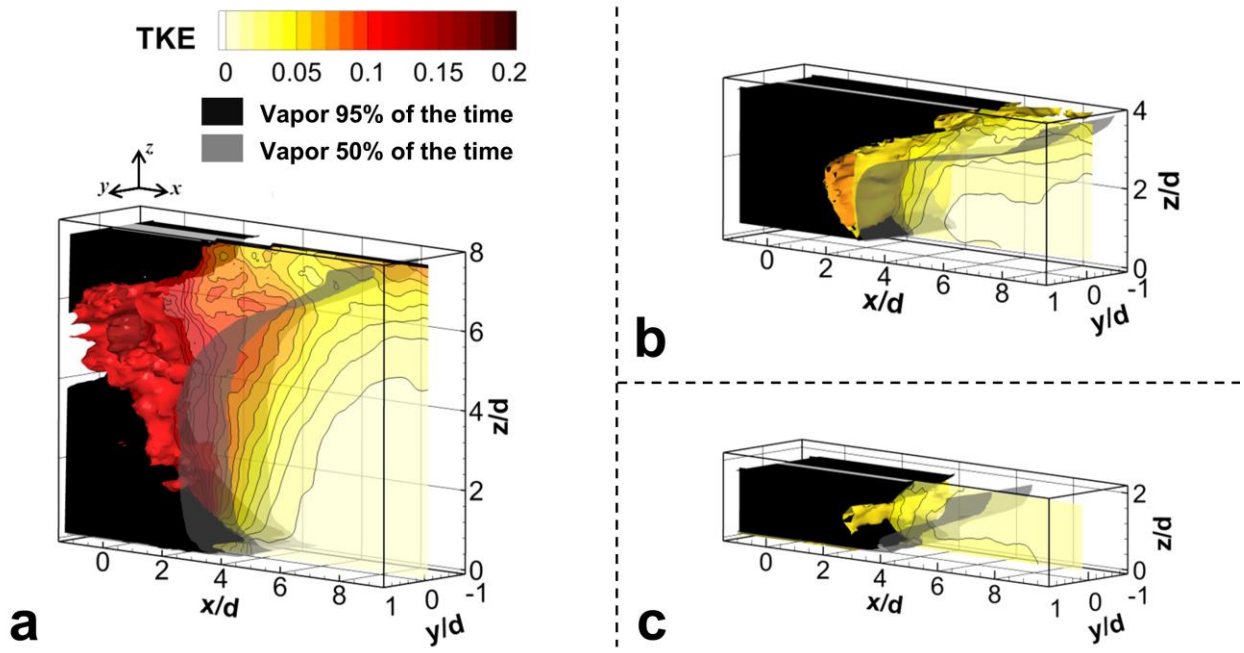

Figure 8. 3D iso-surfaces and contours of turbulent kinetic energy for Re = 5,000 and Bl^* = 1.5 along the y/d = 0 plane for (a) H/d = 8, (b) H/d = 4, and (c) H/d = 2.

with vapor pinch-off at H/d = 8 no longer exists at this spacing. A maximum *TKE* of 0.13 occurs at H/d = 4. The smallest spacing of H/d = 2 (Figure 8c) displays the least intense contours of *TKE*. *TKE* in the confinement gap may therefore be largely characterized as being low in magnitude ($TKE \leq 0.09$).

4.3.2. Vapor-induced coherent structures

The causes of the turbulent kinetic energy distributions in Figure 8 can be further explained by probing the turbulence structure. 3D coherent structures are identified in the liquid using the λ_2-criterion of Jeong and Hussain (1995). In Figure 9-11, representative vapor reconstructions at various time instants are presented with coherent vortices plotted as iso-surfaces of λ_2 = -0.5, colored by normalized vorticity magnitude ($|\omega|$). Supplementary time-animation videos of these figures are available online.

Figure 9 shows six time steps of the vapor plume evolution at H/d = 8. Vortices form near the surface of the vapor plume (large vortices are circled in black in the figure). As the vapor plume evolves, vortices develop along the vapor interface. Near the top of the confinement gap, these vortices move outward

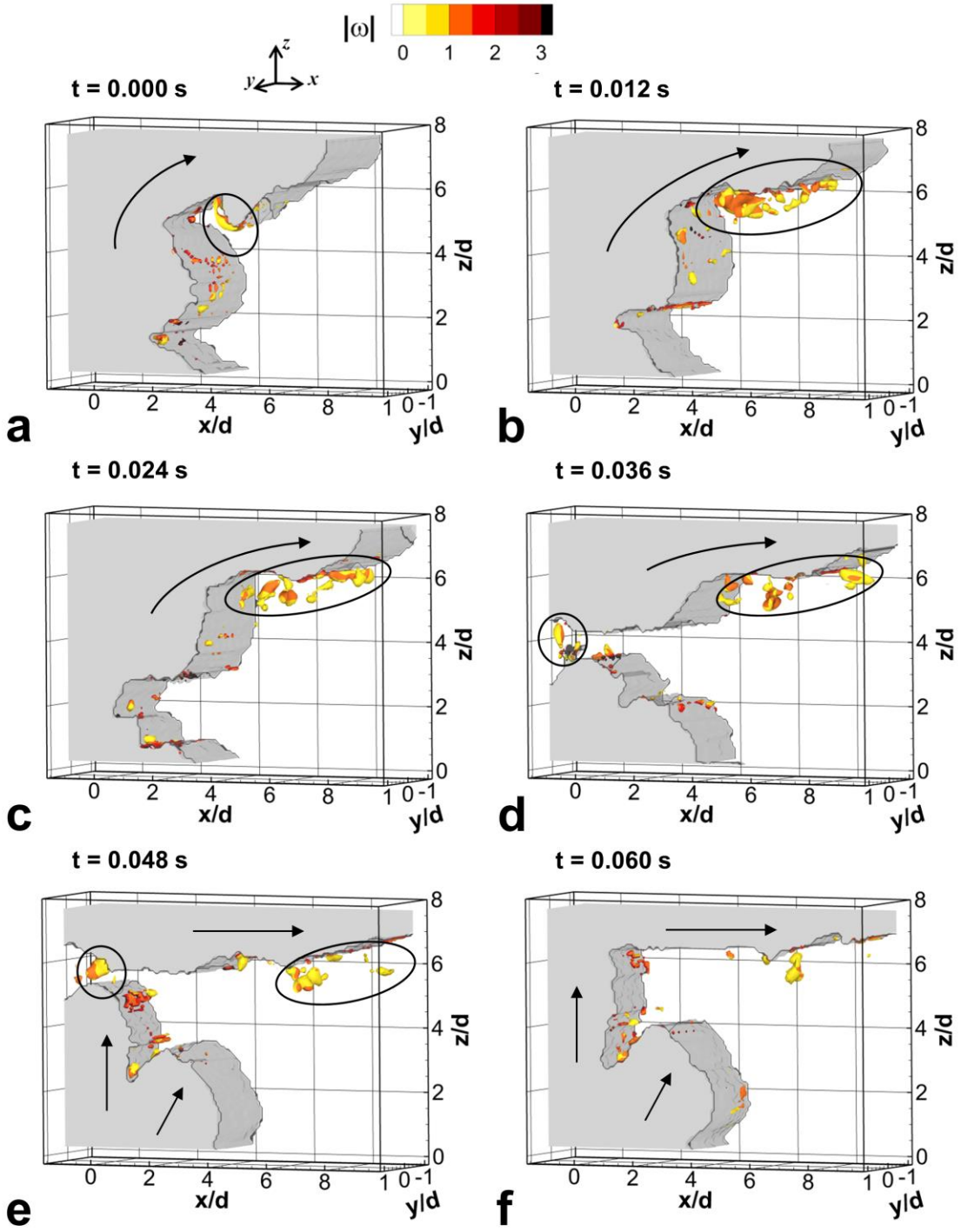

Figure 9. (a)-(f) Vapor evolution with time at a confinement gap height of H/d = 8 for Re = 5,000 and Bl^* = 1.5. Iso-surfaces of λ_2 = -0.5 are plotted and colored by vorticity magnitude. Arrows indicate direction of vapor motion. Supplementary video available online.

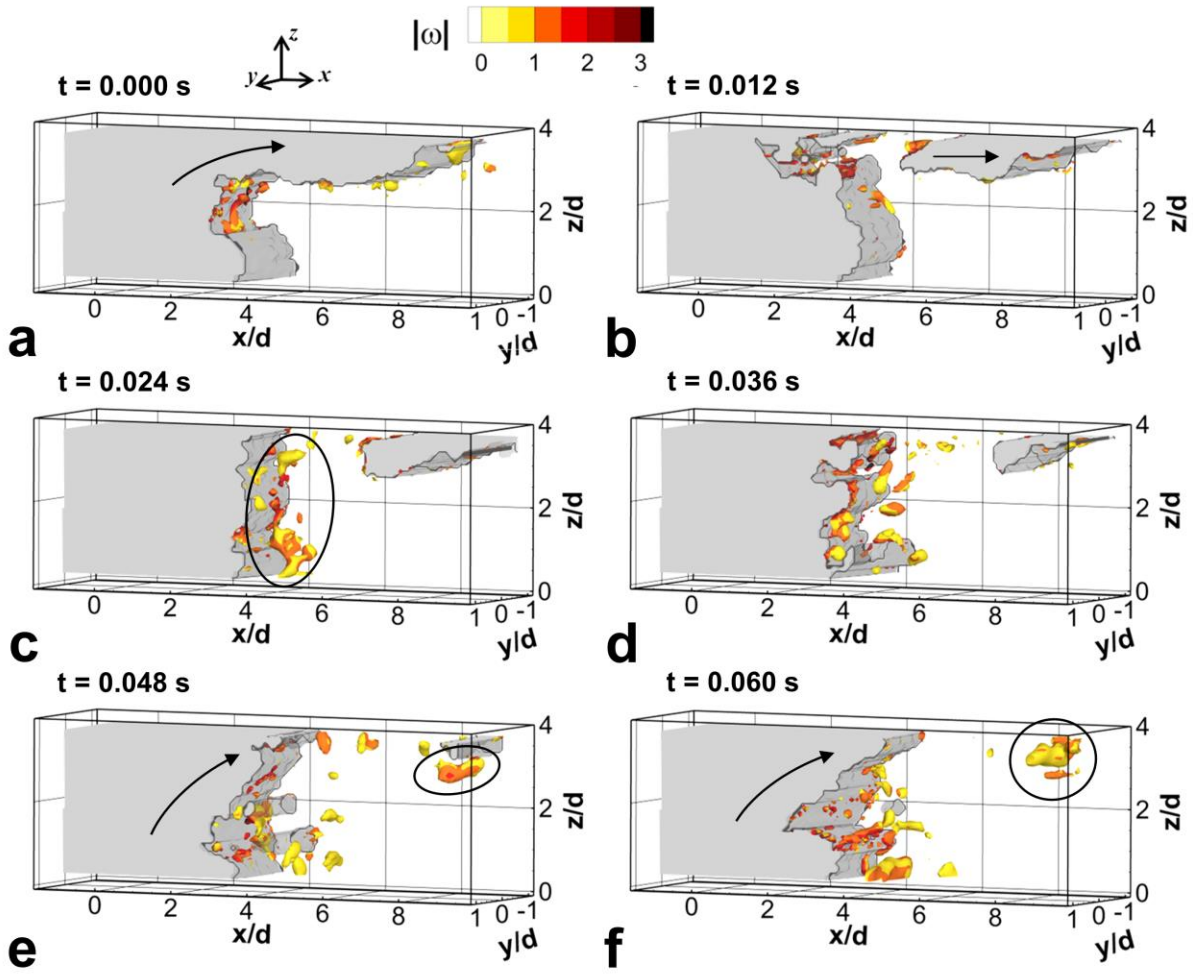

Figure 10. (a)-(f) Vapor evolution with time at a confinement gap height of H/d = 4 for Re = 5,000 and Bl^* = 1.5. Iso-surfaces of λ_2 = -0.5 are plotted and colored by vorticity magnitude. Arrows indicate direction of vapor motion. Supplementary video available online.

following the vapor and liquid motion in this region and slowly dissipate. When the plume pinches off at t = 0.036 s (Figure 9d) additional vortices are created in the resulting void. These structures are destroyed once the separate vapor regions merge into a single plume structure, as shown in Figure 9f.

At H/d = 4 (Figure 10), a bubble is shown to break off from the main plume before moving outward along the top wall, causing the surface of the vapor plume to recoil (Figure 10b). Subsequently, vortices are formed in the liquid near the fluctuating vapor interface and in the wake of the departing bubble. A large vortex can be seen to develop behind the bubble as it leaves the confinement gap in the supplementary video file. The vortex circled in black in Figure 10e and f is a remnant of this motion.

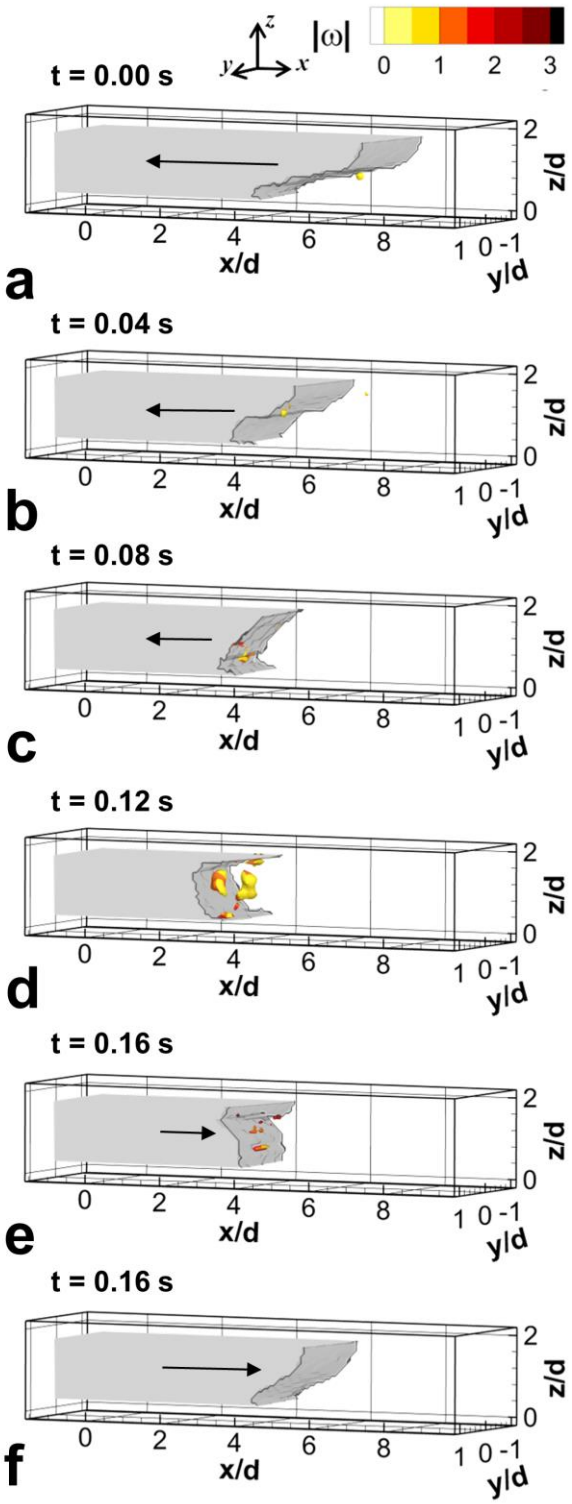

Figure 11. (a)-(f) Vapor evolution with time at a confinement gap height of H/d = 2 for Re = 5,000 and Bl^* = 1.5. Iso-surfaces of λ_2 = -0.5 are plotted and colored by vorticity magnitude. Arrows indicate direction of vapor motion. Supplementary video available online.

Figure 11 shows the vapor motion at $H/d = 2$. The confined vapor plume at this spacing (shown in Figure 5c) grows until one side of the plume reaches an edge of the confinement gap. The time instants in Figure 11a-c show the vapor as it is exiting the left side of the confinement gap (out of the measurement domain); thus, the visible portion of the plume retracts towards the heat source before again growing through the measurement domain in Figure 11e and f. Vortices are absent in the flow shown at this spacing except for when the plume is at its most retracted position between $t = 0.08$ s and 0.18 s, as shown in the supplementary video file and at the time step of $t = 0.12$ s in Figure 11d. A lack of vortices is characteristic of the relatively slow retraction and growth of the plume at this spacing, which is in contrast with the chaotic, vortex-generating motion of the vapor at the larger confinement gap heights.

A statistical representation of vortical structures in the flow is shown Figure 12. The contours indicate the percentage of the time for which $\lambda_2 < -0.5$, indicating the presence of coherent structures. Contour values through the measurement depth are projected onto one plane for plotting and shown with the average plume position as the thick black line. Vortices occur most frequently at $H/d = 8$ and $H/d = 4$ (Figure 12a and b) with maximum values of 57% for $H/d = 8$ (at $r/d = 4$, $z/d = 4$) and 45% for $H/d = 4$ ($r/d = 3.5$, $z/d = 1.6$). The distribution of vortices in the flow is concentrated near the average plume position at these confinement gap heights. In contrast, very few vortices are observed at $H/d = 2$ (Figure 12c), with a maximum occurrence of only 11%.

Comparing Figure 12 with Figure 8, it is evident that vortices are not concentrated in the regions where the most intense *TKE* is observed. *TKE* is highest in the region where pinch-off occurs at $H/d = 8$ (Figure 8a). Vortices form near the vapor interface due to the plume motion (as shown in Figure 9) and are instead most concentrated near the average plume position (as shown in Figure 12). Thus, irrotational liquid displacement caused by pinch-off, rather than coherent vortices, is the main source of *TKE* in this flow. This conclusion is similar to the findings of Lance and Bataille (1991), who found that irrotational perturbations due to the helical motion of the ellipsoidal bubbles in their upward bubbly flow experiments were the dominant cause of increased turbulent energy. Given the large size of the vapor structures in the present study, this conclusion also agrees with the conclusion that irrotational fluctuations have a larger

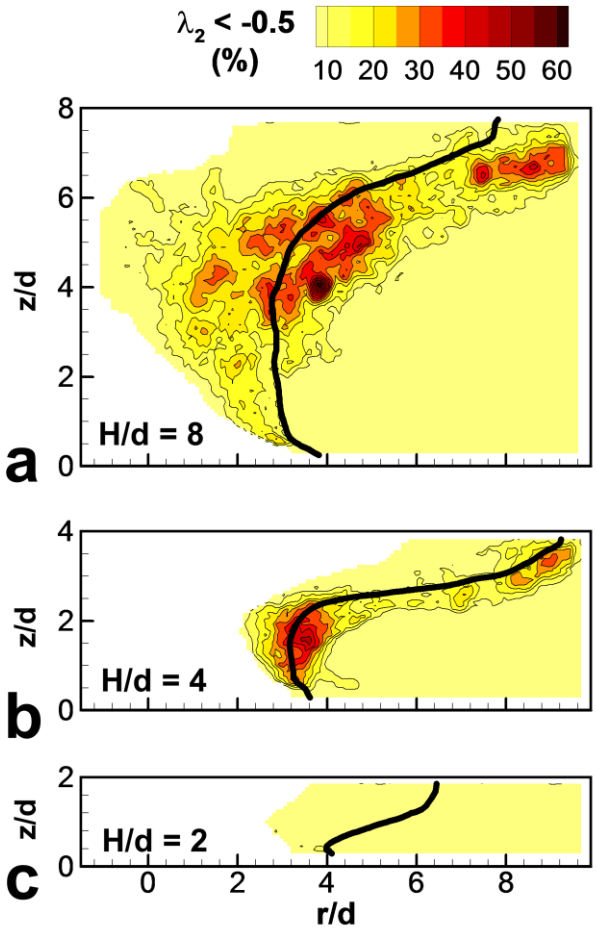

Figure 12. Statistical mappings of the occurrence of coherent structures in the confinement gap for Re = 5,000 and *Bl** = 1.5 at (a) *H*/*d* = 8, (b) *H*/*d* = 4, and (c) *H*/*d* = 2. The 50% plume position is indicated with the thick black line.

effect on *TKE* compared to vortices when the gas phase components are large in size (Bunner and Tryggvason, 2002).

4.4. Vapor volume effects on downstream unsteadiness

Coherent vortices and *TKE* are most prevalent at the larger confinement gap heights; however, bulk flow oscillations can cause additional unsteadiness when boiling occurs in narrow gaps. These oscillations can potentially lead to flow instabilities (Boure *et al*., 1973). To quantify these effects, the instantaneous radial mass flux ($g = \rho v_r$) near the edge of the confinement gap (r/d = 8) is normalized with

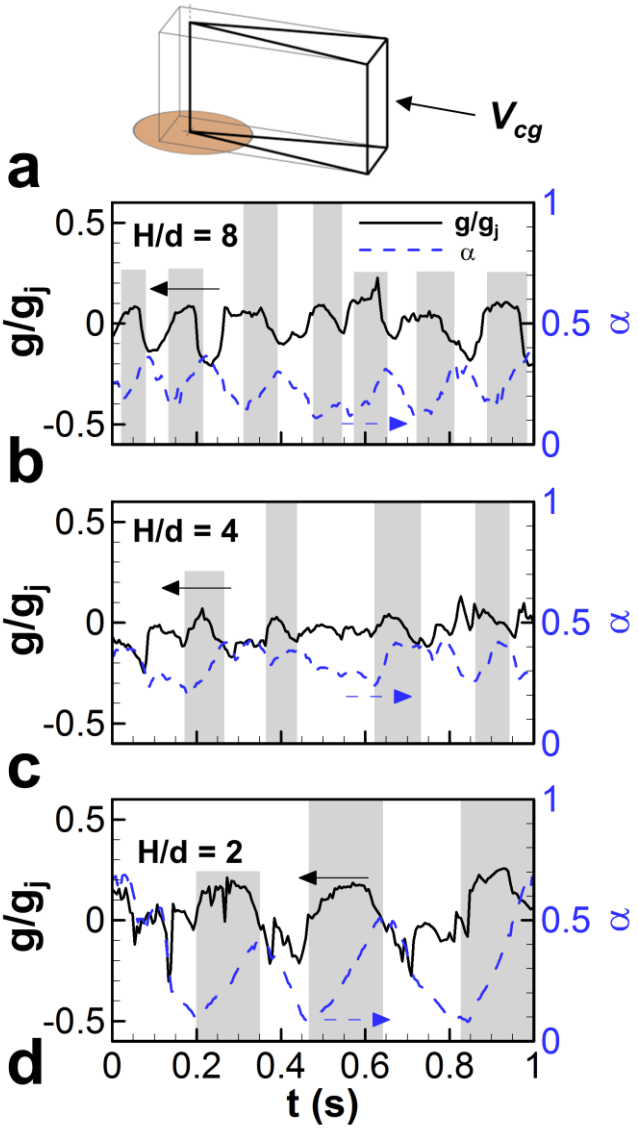

Figure 13. (a) Definition of V_{cg} for the void fraction calculation. Liquid mass flux across the confinement gap edge plotted with vapor void fraction as a function of time for (b) H/d = 8, (c) H/d = 4, and (d) H/d = 2. Grey shading indicates sections where increasing void fraction and peaks in mass flux coincide.

the mass flux of the jet (g_j), and plotted in Figure 13 as a function of time (sign indicates flow direction). The radial mass flux is calculated by integrating the radial velocities across the measurement depth and height. The vapor void fraction is also estimated by determining the volume of the visual hull reconstruction (V_{vapor}) contained within the wedge (V_{cg}) bound by the confinement gap top and bottom

walls and the sector centered at the jet axis within the illumination volume , shown in Figure 13a. The estimated void fraction is then calculated as $\alpha = V_{vapor}/V_{cg}$.

The liquid mass flux at the confinement gap edge displays strongly unsteady behavior with time, as shown in Figure 13. The variations are most extreme at $H/d = 2$ (Figure 13d), where the normalized mass flux has a standard deviation of 0.12. In contrast, the standard deviations at the larger spacings are 0.06 and 0.09 for the $H/d = 4$ and $H/d = 8$ confinement gaps, respectively. The void fraction also changes most drastically at $H/d = 2$, varying from $\alpha = 0.1$ to 0.7 and displays a marked periodic signal with a phase offset from the mass flux. Peaks in radial mass flux occur as the vapor volume increases; sections in the plot where a peak in the mass flux coincides with an increase in void fraction are indicated by the shaded gray regions of the plot.

The cross-correlation coefficient between the mass flux and time-derivative of void fraction $\left(d\alpha/dt\right)$ is obtained to indicate the strength of the correlation between the change in void fraction and the measured radial mass flux. The signals cross-correlate with coefficients of 0.51, 0.32, and 0.22 for the confinement gap heights of $H/d = 2$, 4, and 8, respectively. Correlation coefficients can vary between 0 and 1, with 1 indicating complete correlation. The smallest gap height of $H/d = 2$ has the largest correlation coefficient, indicating that as the confinement gap height is reduced, the vapor growth characteristics have a greater influence on the bulk liquid flow in the gap.

Conclusions

Tomographic PIV measurements of the liquid flow in the confinement gap of two-phase jet impingement are performed at three different gap heights ($H/d = 8$, 4, and 2) for a jet Reynolds number of 5,000. Results are presented at $Bl^* = 0$ (single-phase operation) and $Bl^* = 1.5$, where large vapor bubbles form a plume-like structure above the heated surface. Visual-hull reconstructions of the vapor-phase allow masking of the liquid velocity vectors and an estimation of the vapor void fraction within the confinement gap.

The motion of the vapor plume is shown to govern the time-averaged liquid flow in the confinement gap at all three confinement gap heights investigated. At spacings of $H/d = 8$ and $H/d = 4$, liquid flow patterns follow the vapor motion in the gap with the highest average liquid velocities occurring within the average plume position. Vapor growth and pinch-off at the spacing of $H/d = 8$ cause high liquid velocities and augment circumferential motion. At $H/d = 2$, the vapor plume is confined by the top and bottom walls, which results in less chaotic plume motion and lower-magnitude average liquid velocities.

Coherent vortices within the liquid form due to the motion of the vapor interface. *TKE* is found to be most affected by irrotational liquid displacement due to vapor pinch-off, rather than from the presence of coherent structures in the liquid. In contrast with the larger spacings, few coherent structures are formed in the liquid at $H/d = 2$.

The gap height of $H/d = 2$ displays the largest temporal variation in downstream radial mass flux compared to the larger gaps. Time-resolved analysis reveals that the confined vapor growth dynamics at this spacing correlate with the large-amplitude oscillations in the mass flux. Relatively smaller-amplitude oscillations at the larger gap heights are a result of the entrainment due to pinch-off rather than confined growth of the vapor plume.

Time-resolved tomographic PIV is applied to a flow boiling application for the first time in this work. When combined with simultaneous reconstruction of vapor regions, this technique has the capability of measuring the three-dimensional interaction of turbulent liquid with vapor structures in the flow. Further development of this experimental technique with superior vapor-reconstruction strategies will allow its application to more complex dispersed multiphase flow situations and yield further insights into turbulent multiphase flows.

References

Adhikari, D., Gemmell, B.J., Hallberg, M.P., Longmire, E.K., Buskey, E.J., 2015. Simultaneous Measurement of 3D Zooplankton Trajectories and Surrounding Velocity Field in Complex Flows, J. Exp. Biol. 218, 3534-3540.

Adhikari, D., Longmire, E.K., 2012. Visual hull method for tomographic PIV measurement of flow around moving objects, Exp. Fluids 53, 943-964.

Adhikari, D., Longmire, E.K., 2013. Infrared tomographic PIV and 3D motion tracking system applied to aquatic predator-prey interaction, Meas. Sci. Technol. 24, 024011.

Atkinson, C., Soria, J., 2009. An efficient simultaneous reconstruction technique for tomographic particle image velocimetry, Exp. Fluids 47, 553-568.

Boure, J.A., Bergles, A.E., Tong, L.S., 1973. Review of two-phase flow instabilities, Nucl. Eng. Des. 25, 165-192.

Brücker, C., 1999. Structure and dynamics of the wake of bubbles and its relevance for bubble interaction, Phys. Fluids 11, 1781-1796.

Bunner, B., Tryggvason, G., 2002. Dynamics of homogeneous bubbly flows Part 2. velocity fluctuations, J. Fluid Mech. 466, 53-84.

Charonko, J.J., Vlachos, P.P., 2013. Estimation of uncertainty bounds for individual particle image velocimetry measurements from cross-correlation peak ratio, Meas. Sci. Technol. 24, 065301.

Elsinga, G.E.Scarano, F., Wieneke, B., van Oudheusden, B.W., 2006. Tomographic particle image velocimetry, Exp. Fluids 41, 933-947.

Fitzgerald, J.A., Garimella, S.V., 1997. Flow field effects on heat transfer in confined jet impingement, J. Heat Transf. 119, 630-632.

Fitzgerald, J.A., Garimella, S.V., 1998. A study of the flow field of a confined and submerged impinging jet, Int. J. Heat Mass Tran. 41, 1025-1034.

Fujiwara, A., Danmoto, Y., Hishida, K., Maeda, M., 2004. Bubble deformation and flow structure measured by double shadow images and PIV/LIF, Exp. Fluids 36, 157-165.

Gemmell, B.J., Adhikari, D., Longmire, E.K., 2014. Volumetric quantification of fluid flow reveals fish's use of hydrodynamic stealth to capture evasive prey, J. R. Soc. Interface 11, 20130880.

Garimella, S.V., 2000. Heat transfer and flow fields in confined jet impingement, Ann. Ref. Heat Transfer 11, 413-494.

Hassan, Y.A., Blanchat, T.K., Seeley, C.H., Canaan, R.E., 1992. Simultaneous velocity measurements of both components of a two-phase flow using particle image velocimetry, Int. J. Multiphase Flow 18, 371-395.

Hassan, Y.A., Ortiz-Villafuerte, J., Schmidl, W.D., 2001. Three-dimensional measurements of single bubble dynamics in a small diameter pipe using stereoscopic particle image velocimetry, Int. J. Multiphas. Flow 27, 817-842.

Jeong, J., Hussain, F., 1995. On the identification of a vortex, J. Fluid Mech. 285, 69-94.

Lance, M., Bataille, J., 1991. Turbulence in the liquid phase of a uniform bubbly air-water flow, J. Fluid Mech. 222, 95-118.

Lindken, R., Merzkirch, W., 2002. A novel PIV technique for measurements in multiphase flows and its application to two-phase bubbly flows, Exp. Fluids 33, 814-825.

Lynch, K., Scarano, F., 2013. A high-order time-accurate interrogation method for time-resolved PIV, Meas. Sci. Technol. 24, 035305.

Murphy, D.W., Webster, D.R., Yen, J., 2012. A high-speed tomographic PIV system for measuring zooplanktonic flow, Limnol. Oceanogr.: Methods. 10, 1096-1112.

Prasad, A.K., Jensen, K., 1995. Scheimpflug stereocamera for particle image velocimetry in liquid flows, Appl. Optics 34, 7093-7099.

Rau, M.J., Garimella, S.V., 2013. Local two-phase heat transfer from arrays of confined and submerged impinging jets. Int. J. Heat Mass Tran. 67, 487-498.

Rau, M.J., Garimella, S.V., 2014. Confined jet impingement with boiling on a variety of enhanced surfaces. J. Heat Transf. 136, 101503.

Rau, M.J., Garimella, S.V., Dede, E.M., Joshi, S.N., 2015. Boiling heat transfer from an array of round jets with hybrid surface enhancements. J. Heat Transf. 137, 071501.

Rau, M.J., Guo, T., Vlachos, P.P., Garimella, S.V., 2016. Stereo-PIV measurements of vapor-induced flow modifications in confined jet impingement boiling, Int. J. Multiphas. Flow, in review.

Rieger, J., 1996. The glass transition temperature of polystyrene, J. Thermal Analysis, 46, 965-972.

Roy, R.P., Hasan, A., Kalra, S.P., 1993. Temperature and velocity fields in turbulent liquid flow adjacent to a bubbly boiling layer, Int. J. Multiphase Flow 19, 765-795.

Roy, R.P., Velidandla, V., Kalra, S.P., 1997. Velocity field in turbulent subcooled boiling flow, J. Heat Transf. 119, 754-766.

Scarano, F., 2013. Tomographic PIV: principles and practice, Meas. Sci. Technol. 24, 012001.

Sciacchitano, A., Wieneke, B., Scarano, F., 2013. PIV uncertainty quantification by image matching, Meas. Sci. Technol. 24, 045302.

Serizawa, A., Kataoka, I., 1990. Turbulence suppression in bubbly two-phase flow, Nucl. Eng. Des. 122, 1-16.

Theofanous, T.G., Sullivan, J., 1982. Turbulence in two-phase dispersed flows, J. Fluid Mech. 116, 343-362.

Timmins, B.H., Wilson, B.W., Smith, B.L., Vlachos, P.P., 2012. A method for automatic estimation of instantaneous local uncertainty in particle image velocimetry measurements, Exp. Fluids 53, 1133-1147.

Tokuhiro, A., Fujiwara, A., Hishida, K., Maeda, M., 1999. Measurement in the wake region of two bubbles in close proximity by combined shadow-image and PIV techniques, J. Fluid. Eng. 121, 191-197.

Tokuhiro, A., Maekawa, M., Iizuka, K., Hishida, K., Maeda, M., 1998. Turbulent flow past a bubble and an ellipsoid using shadow-image and PIV techniques, Int. J. Multiphas. Flow 24, 1383-1406.

Violato, D., Ianiro, A., Cardone, G., Scarano, F., 2012. Three-dimensional vortex dynamics and convective heat transfer in circular and chevron impinging jets, Int. J. Heat Fluid Fl. 37, 22-36.

Violato, D., Scarano, F., 2011. Three-dimensional evolution of flow structures in transitional circular and chevron jets, Phy. Fluids 23, 124104.

Weiland, C., Vlachos, P.P., 2013. Round gas jets submerged in water, Int. J. Multiphas. Flow 48, 46-57.

Wieneke, B., 2008. Volume self-calibration for 3D particle image velocimetry, Exp. Fluids 45, 549-556.

Xue, Z., Charonko, J.J., Vlachos, P.P., 2015. Particle image pattern mutual information and uncertainty estimation for particle image velocimetry, Meas. Sci. Technol. 26, 074001.

List of Figures

and (d) $H/d = 2$. Grey shading indicates sections where increasing void fraction and peaks in mass flux coincide.